

# Nanoscale

Accepted Manuscript



This is an *Accepted Manuscript*, which has been through the Royal Society of Chemistry peer review process and has been accepted for publication.

*Accepted Manuscripts* are published online shortly after acceptance, before technical editing, formatting and proof reading. Using this free service, authors can make their results available to the community, in citable form, before we publish the edited article. We will replace this *Accepted Manuscript* with the edited and formatted *Advance Article* as soon as it is available.

You can find more information about *Accepted Manuscripts* in the [Information for Authors](#).

Please note that technical editing may introduce minor changes to the text and/or graphics, which may alter content. The journal's standard [Terms & Conditions](#) and the [Ethical guidelines](#) still apply. In no event shall the Royal Society of Chemistry be held responsible for any errors or omissions in this *Accepted Manuscript* or any consequences arising from the use of any information it contains.

Cite this: DOI: 10.1039/c0xx00000x

www.rsc.org/xxxxxx

ARTICLE TYPE

# Progress in preparation and application of three-dimensional graphene-based porous nano composites

Zhengquan Yan<sup>a,c</sup>, Wenli Yao<sup>b</sup>, Lei Hu<sup>a</sup>, Dandan Liu<sup>a</sup>, Chundong Wang<sup>c</sup>, Chun-Sing Lee<sup>\*c</sup>

Received (in XXX, XXX) XthXXXXXXXXXX 20XX, Accepted Xth XXXXXXXXXXXX 20XX

DOI: 10.1039/b000000x

Due to the high specific surface area, excellent conductivity, low mass density, good compatibility and elegant flexibility, three-dimensional graphene composites with interconnected porous structures possess unusual and novel physical and electronic properties, unsurpassed chemical functionalities and other attractive features. Therefore, different three-dimensional graphene-based nano porous scaffolds have been extensively designed, prepared and investigated for practical applications in lithium-ion batteries, super-capacitors, solar cells, catalysis, thermal management, environment pollution enrichment and separation, and chemical sensors with high performances from both fundamental and technological viewpoints. To present the readers a better understanding of this kind of important porous materials, in this feature article, we will highlight the main achievements made for preparing 3D graphene micro- and/or nano-architectures and their potential applications in the fields as aforementioned.

## 1. Introduction

Graphene, a two-dimensional (2D) monolayer sheet of hexagonal sp<sup>2</sup>-hybridized carbon atoms arranged in a honeycomb lattice, has attracted extreme attention since its experimental discovery in 2004.<sup>1</sup> Owing to its remarkable properties, such as large specific surface area, excellently electrical and thermal conductivity, good light transmission, high mechanical strength, graphene-based materials have been developed for active materials of energy storage and conversion,<sup>2-7</sup> transparent conductors,<sup>8-11</sup> nanoelectronics,<sup>12-14</sup> and chemical sensors,<sup>15-19</sup> etc. There being strong  $\pi$ - $\pi$  stacking interaction, Van der Waals forces and high surface energy, however, graphene monolayer sheets tend to stack and self-aggregate. So many graphene macro-assemblies with three dimensional (3D) nanostructures have appeared in recent reports using in situ reduction-assembly method,<sup>20, 21</sup> chemical vapor deposition (CVD)<sup>22-24</sup> and template-direction methods.<sup>25,26</sup> 3D graphene porous nano composites with interconnected networks are high conductive and mechanically robust compared with 2D graphene monolayer. Also, the low mass density, high specific surface area, good compatibility and excellent flexibility make 3D graphene networks novel or specially physical and electronic properties, unsurpassed chemical functionality and other attractive features. Now, they have been widely applied in energy storage/conversion,<sup>27, 28</sup> contamination absorbents,<sup>29</sup> catalyses,<sup>30, 31</sup> composites,<sup>32</sup> and chemical sensors<sup>33,34</sup> with better functions than 2D graphene. All these conclusions strongly demonstrated that integrating nano monolayer graphene into macroscopic 3D porous interconnected networks has proved to be a key role to realize their practical applications, through which the properties at the nanoscale could be effectively translated into that on the macroscopic level.

To present the readers a systematic overview, the following sections will highlight the development of preparation and application of 3D graphene-based macroscopic porous composites, based on the work developed during the recent years, which will be different from the previous overviews summarizing 3D graphene architectures comprehensively in the literatures before.<sup>25, 35-37</sup>

## 2. Preparation methods

### 2.1 Self-assembly methods

Self-assembly is a ubiquitous natural phenomenon capable of spontaneously forming multiple ordered structures within a system composing of many individual subunits through non-covalent bonds, such as hydrogen bond, van der Waals force, metalto-ligand bond, electrostatic force, hydrophobic-hydrophilic interaction, and  $\pi$ - $\pi$  stacking interaction.<sup>38-40</sup> Especially, self-assembly could integrate and translate the individuals into the resultant macrostructures with numerous breakthrough and special applications in optoelectronics, energy-storage, biomedicine and environmental pollution separation. For example, Vickery, *et al.*<sup>41</sup> reported two high-order 3D graphene-polymer nanocomposites, *i.e.*, sponge-like macroporous scaffold and hollow micrometer-sized sphere, using template-directed self-assembly methods. As shown in top **Figure 1a**, sponge-like macroporous scaffold could be controllably fabricated by ice-segregation-induced self-assembly. A homogeneous aqueous mixture of poly(vinyl alcohol) (PVA) and polystyrene sulfonate-stabilized graphene sheets (PSS-G) was first transferred into an insulin syringe and frozen by controlled immersion into liquid nitrogen. The frozen scaffold was then freeze-dried to sublime the ice crystals to produce a macro-porous monolith, whose

morphologies could be effectively controlled by immersion rate, graphene concentration and polymer type. On the other hand, PSS-G-coated polymer hollow micro-spheres were constructed by controllably depositing negatively charged PSS-G dispersions on the surface of positively charged polymer beads (down Figure 1a). Subsequently treated with toluene to remove the core template, hollow PSS-G microspheres were produced. This study demonstrates that electrostatically induced assembly is a feasible method for controlling the high-order graphene-based architectures from polymer-stabilized graphene sheets dispersed in aqueous solutions.

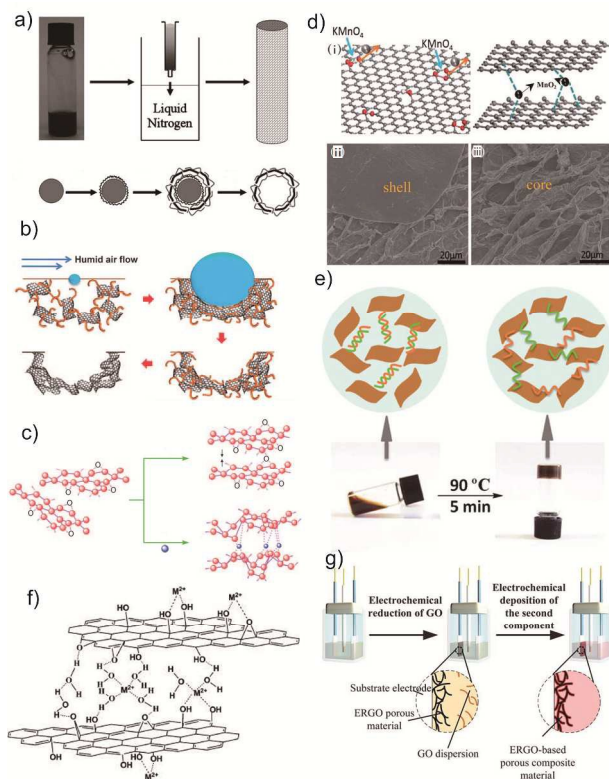


**Figure 1.** The representative self-assembly routes for 3D graphene composites proposed in the literatures<sup>41,42,44-47,49</sup>

Using polystyrene-grafted graphene oxide (GO) as precursors, Lee, *et al.*<sup>42</sup> reported a “breath-figure” method to self-assembly 3D macroporous carbon films with tunable porous morphologies. As shown in **Figure 1b**, the dispersion was cast onto a suitable substrate and exposed to a stream of humid air after GO platelets were dispersed in benzene. Endothermic evaporation of the volatile organic solvent resulted in the spontaneous condensation and close packing of aqueous droplets at the organic solution surface. Subsequently drying the polymer-grafted GO on the substrate, a mechanically flexible and robust macroporous film, comprised of reduced graphene oxide (RGO) platelets, was formed and constructed upon pyrolysis. The pore size and the number of porous layers could be effectively controlled by the concentration of the organic precursor dispersion and the length of polymer chains grafted to the GO surface. Therefore, a more straightforward self-assembly method to fabricate high ordered, mechanically flexible macro-porous RGO assemblies with tunable open porous morphologies was developed. Latest reporter further developed some self-assembled 3D RGO structures via

boiling reduced graphene oxide (RGO) colloidal dispersion accordingly.<sup>43</sup>

Using a hydrothermal method with the assistance of noble-metal nanoparticles (Au, Ag, Pd, Ir, Rh, Pt, *etc.*), Tang, *et al.*<sup>44</sup> described a 3D GO assembly with macro-porous structures as shown in **Figure 1c**. For example, Pd nanoparticles anchored onto GO sheets could act as active sites for self-assembly with another GO sheet. The corrugations formed in the Pd-bearing GO would also result in porous structures, which could be easily controlled by adjusting the volume of the vessel and the effective concentration of GO. The work not only provides a simple way to fabricate porous structures from GO, but also indicates that GO can be self-assembled into more complicated 3D structures with high catalytic activity and selectivity in the chemical reaction for either a fixed- or fluid-bed processes in large-scale production.

Lv, *et al.*<sup>45</sup> developed a one-pot self-assembly process to construct cylinder-like 3D graphene macro-assemblies with core-shell structures below 100 °C at normal atmospheric pressure (**Figure 1d**). Catalyzed by MnO<sub>2</sub> nanoparticles decomposed from KMnO<sub>4</sub>, the self-assembly was effectively to avoid the face-to-face stacking of RGO sheets as shown in Figure 1d (right). What’s more, the porous structure and the size of the assembly can be tuned by changing the KMnO<sub>4</sub> fraction. The one-pot assembled nano-porous carbons with layered shells show potential application in electrochemical energy storage devices.

By heating the mixture of GO aqueous dispersion and double-stranded DNA (dsDNA) aqueous solution (1:1 V/V) at 90 °C for 5 min, Xu, *et al.*<sup>46</sup> prepared a typical GO/DNA composite self-assembled hydrogel. As illustrated in **Figure 1e**, dsDNA was unwound to single-stranded DNA (ssDNA) during the heating process, and then the *in situ* formed ssDNA chains bridged adjacent GO sheets *via* strong noncovalent interactions, such as  $\pi$ - $\pi$  stacking interaction, *etc.* Thus, a stable self-assembled hydrogel was constructed from GO sheets and ssDNA chains. This work provides a new insight for the assembly of functionalized graphene with biomolecules, which will benefit rational design and fabrication of hierarchical graphene-based materials.

By virtue of the chemical bond and hydrogen bond among RGO sheets, divalent metal ions (Ca<sup>2+</sup>, Ni<sup>2+</sup>, or Co<sup>2+</sup>) and water molecules, Jiang, *et al.*<sup>47</sup> assembled RGO sheets into gel-like 3D architectures under hydrothermal treatment (**Figure 1f**). After GO was dispersed into deionized water under sonication, some CaCl<sub>2</sub> with different Ca<sup>2+</sup>/GO weight ratios was added into and stirred for 3 h. The mixture was then treated hydrothermally at 120 °C for 10 h. After the autoclave was cooled down to the room temperature, a black gel-like cylinder was formed in the bottom of the autoclave. Replacing CaCl<sub>2</sub> by NiCl<sub>2</sub> or CoCl<sub>2</sub>, similar RGO cylinders were also obtained. The as-prepared RGO cylinder was immersed in 0.25 wt % PVA (MW~20000) solution for 5 min and then freeze-dried to prepare PVA-strengthened 3D architecture. In the resultant porous structures, RGO sheets, water molecules and divalent ions play the role of skeleton, filler, and linker, respectively. The large amount of water (~99 wt %) in the galleries of RGO sheets can offer many water channels for introducing PVA molecules. It presents a promising potential in preparing versatile 3D RGO-based host-guest composites.

Using covalent carbon cross-links between graphene sheets

instead of common physical bonds, Worsley, *et al.*<sup>26</sup> prepared a kind of 3D graphene aerogel. The GO suspension was gelled via resorcinol-formaldehyde (RF) sol-gel chemistry first. The resulting GO-RF wet gel was then dried and pyrolyzed to produce the graphene aerogel, whose electrical conductivity was orders of magnitude higher than that of graphene aerogel made through physical cross-links alone. Later, using the sol-gel chemistry proposed, they<sup>48</sup> further introduced chemical bonds between graphene sheets to control the bulk properties of graphene-based aerogels. 3D graphene assembly with decreasing RF content possesses a higher degree of exfoliation and less C-H bonding than that with higher RF contents, while maintains the high conductivity.

Chen, *et al.*<sup>49</sup> reported a universal strategy for fabricating 3D porous graphene-based composites with a two-step electrochemical deposition process. As shown in **Figure 1g**, a porous 3D graphene framework was first prepared by electrochemical reduction of GO aqueous solution, and then the second component was incorporated into this 3D framework by in situ electrochemical deposition. Low deposition rate is quite necessary for the uniform deposition of the second component. Recently, through  $\pi$ - $\pi$  stacking interaction, Wang, *et al.*<sup>50</sup> further developed the in situ self-assembly of 3D graphene sheets using the chemical reduction of GO in the presence of natural phenolic acids. This method enjoys low cost, environmentally friendly procedure and mild reaction conditions.

Combining self-assembly with hot press technique, Wu, *et al.*<sup>51</sup> fabricated 3D graphene-polymer composites using polystyrene and ethylene vinyl acetate as raw materials. The obtained composite possessed a higher electrical conductivity than that of the corresponding reported composites chemically functionalized with the same components.<sup>52</sup> Another substrate-assisted GO reduction and assembly method was developed by Hu, *et al.*,<sup>53</sup> without any additional reducing agents on arbitrary substrates. The substrate-assisted assembly method offers a facile and efficient approach to construct a variety of unique graphene assemblies for practical applications.

## 2.2 Chemical vapor deposition (CVD) method

Template-directed chemical vapor deposition is another important and easy method to prepare 3D foam-like graphene macrostructures with entire  $sp^2$ -hybridized carbon atoms. Using this methodology, Chen, *et al.*<sup>54</sup> first reported foam-like graphene macrostructures (GFs) using an interconnected 3D nickel scaffold as a template. As shown in **Figure 2a**, carbon was first introduced and precipitated on the surface of the nickel template by decomposing  $CH_4$  at 1,000 °C under ambient pressure. Owing to the difference between the thermal expansion coefficients of nickel and graphene, ripples and wrinkles could be formed on the graphene films, which resulted in an improved mechanical interlocking and better adhesion with polymer chains to form different functional composites. So poly(methyl methacrylate) (PMMA) was easily deposited on the surface of the graphene films to prevent graphene networks from collapsing before etching away the nickel skeleton by hot HCl (or  $FeCl_3$ ) solution. After the PMMA layer was carefully removed by hot acetone, a monolith of continuous and interconnected 3D graphene network was obtained. The GF copied and inherited the interconnected 3D scaffold structure of the nickel foam template. The as-prepared

GF possesses an electrical conductivity of  $\sim 10 \cdot S \cdot cm^{-1}$ , 6 orders of magnitude higher than that of chemically derived graphene-based composites,<sup>55</sup> due to the interconnected flexible network for the fast transport channel of charge carriers.

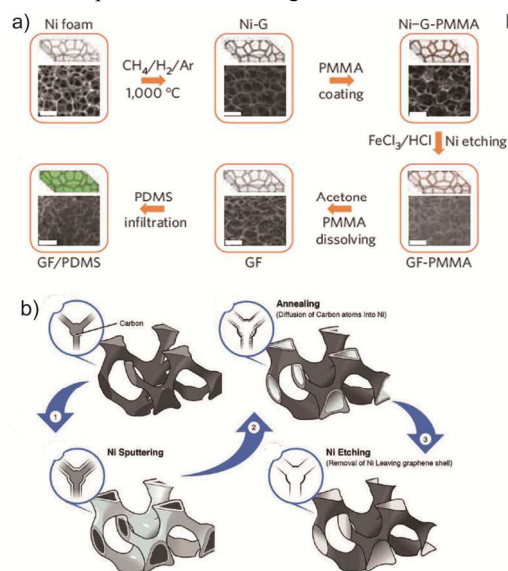


**Figure 2** The representative chemical-vapor-deposition routes for 3D graphene composites proposed in the literatures<sup>54,59</sup>

Using ecofriendly ionic liquids and microwave irradiation as the energy source, Sridhar, *et al.*<sup>56</sup> constructed 3D graphene shell-plate nanostructures with “nano-cup arrays” vertically anchored on few-layered graphene substrates. The synthetic procedure included two simple steps, *i.e.*, one-pot synthesis of composites with metal nanoparticles anchored on the graphene surface, and etching of metals with dilute HCl to result in unique graphene-based shell-plate nano-structures subsequently. It provides a promising and convenient pathway to achieve mass production of 3D graphene with domestic microwave and green ionic liquids.

Recently, using plasma enhanced chemical vapor deposition, our group<sup>57</sup> obtained a 3D graphene scaffold with much larger surface area. When the Ni foam was heated to 550 °C, hydrogen plasma was produced by introducing a 1,300 W microwave power. After the Ni foam scaffold was etched, 3D graphene micro-graphene tube was obtained, which was a bit different from the one grown by Chen, *et al.*<sup>54</sup> *i.e.*, it was a 3D graphene architecture grown on the surface of the 3D graphene scaffold, which was named as a micro-graphene nanotube accordingly.

Using PVA/iron as precursors, Yoon, *et al.*<sup>58</sup> reported a substrate-free CVD method to fabricate 3D graphene composites. The PVA/iron precursor was annealed under a hydrogen environment and then infiltrated into 3D colloidal silica. During the experiment, iron ions were reduced and few-layer graphene was precipitated on the surface of the reduced iron, whose dimension could be effectively tuned by regulating the creation of nano-networks. Importantly, the resultant 3D graphene could be further transferred onto any arbitrary substrate for flexible devices.

Xiao, *et al.*<sup>59</sup> described the conversion of predefined 3D pyrolyzed photoresist films into well-defined 3D porous graphene. The conversion experienced a three-step process as shown in **Figure 2b**, where 3D amorphous carbon structures were

conformably sputtered with nickel and annealed to convert the material into 3D graphene monoliths. After acidic etching to remove the remaining nickel template, hollow and interconnected 3D multilayered graphene structures were chemically converted with pore sizes around 500 nm.

### 2.3 Other methods

It has been discovered that local strain in a graphene sheet can alter its conducting property and transport gap. Based on this point, Li, *et al.*<sup>60</sup> developed a scalably strain-engineering technique to generate 3D graphene nanostructures. Utilizing laser-induced shock pressure, the graphene sheet was conformably pressed onto the mold patterns and taken the shape of the patterns with tunable strains as shown in **Figure 3a**. The process could be scaled up to roll to roll ones by changing laser beam size and scanning speed. The proposed approach possesses a great potential to realize all graphene circuit for applications in various nano-electrical devices.

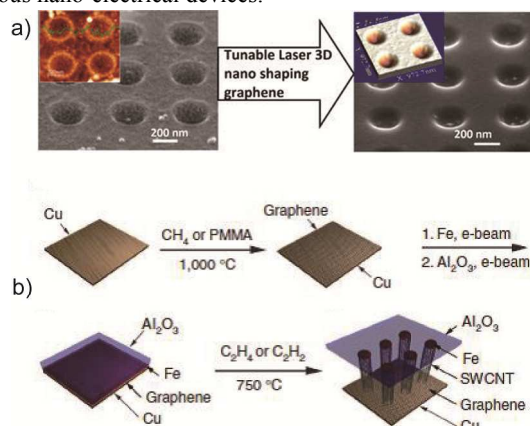


**Figure 3** The other representative routes for 3D graphene composites proposed in the literatures<sup>60,62</sup>

Freeze casting is another template-free strategy for fabricating graphene sponge developed recently. For example, Xie, *et al.*<sup>61</sup> proposed a very convenient and general protocol to finely tailor the porous architecture and property. Using the modified freeze casting process, the resulting pore sizes and wall thicknesses could be gradually tuned from 10 to 800 nm and from 20 to 80 nm, respectively, with corresponding properties changing from hydrophilic to hydrophobic and the Young's Modulus varying by 15 times.

To simultaneously combine the excellent properties of carbon nanotubes (CNTs) and graphene, Zhu, *et al.*<sup>62</sup> devised a sandwich structure using graphene and CNTs through covalent bonds. As shown in **Figure 3b**, graphene was grown on a copper foil by decomposing  $\text{CH}_4$  or PMMA at 1,000 °C. Then the iron catalyst and alumina buffer layer were deposited on the graphene in series by electron beam evaporation. During the process, iron catalyst and alumina buffer layer were lifted up and the CNT carpet was grown directly out of the graphene. There was no barrier between graphene and nanotube carpet. The top alumina layer acted as a floating buffer layer to assist the formation of small-diameter CNT carpets. Not only serving standalone properties, the hybrid material also exhibited a specific surface area of 42,000  $\text{m}^2 \cdot \text{g}^{-1}$  with ohmic contact from the vertically aligned single-walled CNT

to graphene. The work provides a new benchmark to understand the 3D graphene/single-walled CNT-conjoined materials.

Using a uniquely defect-engineered microwave technique, Sridhar, *et al.*<sup>63</sup> grew CNTs on graphene sheets to form 3D carbon nanostructures. The sequential process included defect generation on graphene sheets under microwave irradiation, anchoring of palladium nanoparticles on these defects and growth of carbon nanotubes with the aid of an ionic liquid. The resulting 3D graphene-CNT-palladium composites consisted of carbon nanotubes vertically standing on graphene sheets through covalent bonding and palladium nanoparticles attached at the top of the carbon nanotubes. You, *et al.*<sup>64</sup> further reported 3D N-doped graphene-CNT networks by hydrothermal treatment, freeze-drying and subsequent carbonization of graphene oxide-dispersed pristine CNTs in the presence of pyrrole successively. Its key feature was using GO as "surfactant" to directly disperse pristine CNTs without any additives.

Li, *et al.*<sup>65</sup> reported a one-step ion-exchange/activation method to construct 3D graphene-based materials using a metal ion exchange resin as a carbon precursor at low temperature. The ion-exchange resin containing  $\text{Ni}^{2+}$  decomposed, carbonized, and finally graphitized to generate gaseous CO and  $\text{CO}_2$ , which resulted in porous graphene-like network structures. In the presence of KOH, the graphene-like materials were then activated to form 3D hierarchical porous architectures. The method is simple, scalable and compatible.

Recently, the ordered 3D conjugated polyaniline (PANI)-graphene composites were fabricated by Liu, *et al.*<sup>66</sup> using in-situ chemical oxidative polymerization of aniline in the presence of amino-functionalized graphene sheets. PANI polymerization could be initiated by amino groups on graphene. Also, the density and size of ordered PANI nanorod arrays could be manipulated by controlling the amount of amino-functionalized graphene sheets. Owing to conjugated covalent bonds and ordered PANI nanorod arrays, the resultant composite possessed high special capacitance, low electrical resistance and excellent cycling stability.

## 3. Performances and Applications

### 3.1 Lithium-ion Batteries

The lithium-ion battery (LIB) is one of the most important power sources for portable electronic devices in our daily life. Devising and exploring new electrode materials with high conductivity is an urgent task in constructing next-generation high-performance LIBs. By virtue of its excellent conductivity, large surface area, high stability and mechanical robustness, 3D graphene-based porous materials with interconnected networks have been a promising candidate for high-performance LIBs.

Tang, *et al.*<sup>67</sup> reported 3D porous graphene networks decorated with  $\text{LiFePO}_4$  as electrodes for LIBs. Due to the incorporation of 3D graphene networks,  $\text{LiFePO}_4$ -based composites exhibited high conductivity of  $\sim 600 \cdot \text{S} \cdot \text{cm}^{-1}$ , low square resistance of  $1.6 \cdot \Omega \cdot \text{sq}^{-1}$  and excellent rate performance of  $109 \cdot \text{mA} \cdot \text{h} \cdot \text{g}^{-1}$  at 10 C, indicating a promising application in high-performance LIBs. Later, Ding, *et al.*<sup>68</sup> further confirmed the application of 3D graphene/ $\text{LiFePO}_4$  composites for flexible LIBs. Even with low graphene contents, the composites exhibited a high capacity of

163.7 mA·h·g<sup>-1</sup> at 0.1 C and 114 mA·h·g<sup>-1</sup> at 5 C without further incorporating any other conductive agents. The similar result was also confirmed by Kuo, *et al.*<sup>69</sup>

Using mesoporous TiO<sub>2</sub> submicrospheres embedded in 3D RGO networks (MTO/3D-GN), Yu, *et al.*<sup>70</sup> developed a novel electrode for LIBs. As shown in **Figure 4**, even at a high current rate of 20 C, MTO/3D-GN still possessed a favorable reversible capacity of 124 mA·h·g<sup>-1</sup>, while MTO-G and pure mesoporous TiO<sub>2</sub> only exhibited capacities of 81 mA·h·g<sup>-1</sup> and 38 mA·h·g<sup>-1</sup>, respectively. The cycling performance and rate capability of MTO/3D-GN at each rate were also superior to those of MTO-G and pure mesoporous TiO<sub>2</sub> without RGO support. The action mechanism might be that MTO/3D-GN provided a high contact area between the electrolyte and electrode, favorable diffusion kinetics for both electrons and lithium ions, double protection against the volume changes of electro-active TiO<sub>2</sub> materials and the excellent electrical conductivity of the overall electrode during electrochemical processes.

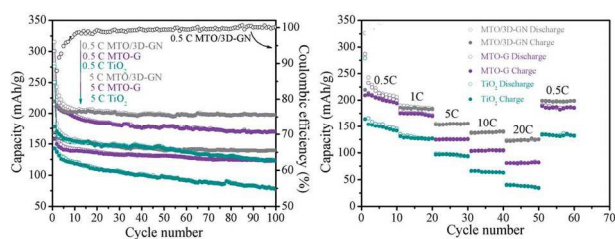


**Figure 4** (left) Cycling performance of pure TiO<sub>2</sub>, TiO<sub>2</sub>-G mixture and the MTO/3D-GN composite at the current rates of 0.5 C and 5 C, respectively. (right) Cycling performance at different current rates from 0.5 C to 20 C of pure TiO<sub>2</sub>, TiO<sub>2</sub>-G mixture and the MTO/3D-GN composite.<sup>70</sup>

By depositing MoS<sub>2</sub> on the surface of 3D graphene networks, Cao, *et al.*<sup>71</sup> demonstrated a binder-free anode for LIBs. The as-prepared anode possessed excellent electrochemical performances, *i.e.*, reversible capacities of 877 and 665 mA·h·g<sup>-1</sup> during the 50th cycle at current densities of 100 and 500 mA·g<sup>-1</sup>, and a 10th-cycle capacity of 466 mA·h·g<sup>-1</sup> at a high current density of 4 A·g<sup>-1</sup>, respectively. What's more, the interconnected porous 3D graphene networks saving as effective pathways for electronic and Li<sup>+</sup> ion exchange, there was no need to add any other conductive additives for constructing LIBs.

Fe<sub>3</sub>O<sub>4</sub> has always been regarded as a promising anode material for LIBs except for its poor cyclability and low rate capability. To overcome this shortcoming, Luo, *et al.*<sup>72</sup> developed a bi-continuous mesoporous Fe<sub>3</sub>O<sub>4</sub> attached onto 3D GFs and utilized it directly as the LIB anode. The resultant anode exhibited a high capacity of 785 mA·h/g at 1C rate without decay up to 500 cycles. It may be the best rate performance reported for Fe<sub>3</sub>O<sub>4</sub> used in LIBs by then.

Chen, *et al.*<sup>73</sup> constructed a multi-walled carbon nanotube/sulfur (MWCNT@S) composite with core-shell structure, which was further embedded into the interlay galleries of graphene sheets (GS). The cathode for Li/S batteries with this composite expressed a higher initial capacity of 1396 mA·h/g at a current density of 0.2 C comparing to the corresponding ones without GS or MWCNT.<sup>74</sup> The synergistic effects between GS and MWCNTs provides a 3D conductive network for electron transfer, open

channels for ion diffusion, strong confinement for soluble polysulfides, and effective buffer for volume expansion of the S-containing cathode during discharge.

Near recently, Ye, *et al.*<sup>75</sup> reported a 3D interconnected network of GAs with lattice defects introduced by 3 MeV He ion bombardment. Used as anodes for LIBs under the same condition, the resultant 3D GAs showed drastically different charge/discharge behavior from that of graphite. The initial lithiation capacity and the reversible capacity of 3D GAs were ~3200 mAh/g [nearly one order of magnitude higher than that of graphite (~372 mAh/g)] and ~770 mAh/g (twice the value of graphite) at the same conditions, respectively. What's more, the capacity of 3D GAs could be obtained mainly below the discharge voltage of 1.0 V, whereas little capacity would be observed between 0.5 and 1.0 V discharge potential in graphite. The study indicated first the importance of defect types to affect the lithium storage capacity of graphene materials.

Our group also devotes to construct 3D graphene-based composites for LIBs. For example, a novel Sn-3D graphene anode was designed, which possessed excellent electrochemical performances and a dramatic improvement in the aspects of capacity, cycle life, and rate capacity with very high reversible capacity and long cycling life.<sup>76</sup> The Sn-3D graphene electrode delivered a reversible capacity of 794 mA·h·g<sup>-1</sup> under 1/3 C for 400 cycles with over 100% capacity retention and 466 mA·h·g<sup>-1</sup> under 1 C for 4000 cycles with 100% capacity retention. The superior performance could be attributed to the unique architecture, intrinsic flexibility, and high conductivity of the designed 3D foothill-like graphene scaffold. On the basis of this work, another anode for LIBs was further developed using 3D Si thin films supported on a graphene scaffold.<sup>2</sup> Owing to the good electrical conductivity and excellent mechanical flexibility of 3D graphene scaffold, the Si anode exhibited a gravimetric capacity as high as 1560 mA·h·g<sup>-1</sup> at a current density of 797 mA·g<sup>-1</sup> and a capacity retention of 84% after 500 cycles relative to the capacity value in the 50th cycle. Meanwhile, specific capacities of 1083 and 803 mA·h·g<sup>-1</sup> were demonstrated after 1200 cycles at 2390 mA·g<sup>-1</sup> and 7170 mA·g<sup>-1</sup>, respectively. All the studies will pave a new way for preparing 3D Si-graphene hybrid structures as robust and scalable Si-based anodes for all-solid-state thin film LIBs.

### 3.2 Super-capacitors

Super-capacitors are a kind of important energy-storage devices since they can deliver orders of magnitude higher power density, cycle efficiency, and charge/discharge rates than a common battery. 3D graphene nano-structures represent a new class of ultralight and porous carbon materials that are associated with high strength-to-weight and surface-area-to-volume ratios. More importantly, interconnected 3D porous networks can provide multidimensional electron transport pathways, easy access to the solid-state electrolyte, and minimized transport distances between bulk electrode and electrolyte. All the features strongly suggest that 3D porous graphene composites could be qualified for application as super-capacitor electrodes.

Fan, *et al.*<sup>77</sup> for the first time, applied 3D CNT/graphene sandwich structures, with CNT pillars grown between the graphene layers, as super-capacitor electrodes. The unique structure endowed the electrode with a high-rate transportation of

electrolyte ions and electrons, resulting in a specific capacitance of  $385 \text{ F}\cdot\text{g}^{-1}$  at  $10 \text{ mV}\cdot\text{s}^{-1}$  in  $6 \text{ M KOH}$  solution. Importantly, the electrode possessed excellent electrochemical stability. For example, the capacitance increased by *ca.* 20% comparing with the initial one even after 2000 cycles. By controlling the lengths of vertical CNT forests emanated from the graphene surface, Yan, *et al.*<sup>78</sup> prepared 3D seamless metal-graphene-CNT hybrids on porous nickel substrates. The resulting 3D porous seamless structure effectively overcame inadequate CNT-metal-electrode contact, low surface-area-utilization efficacy and post-transfer difficulties. The high-performance capacitor was further confirmed by You, *et al.*<sup>64</sup> using 3D N-doped graphene-CNT networks as super-capacitor electrodes.

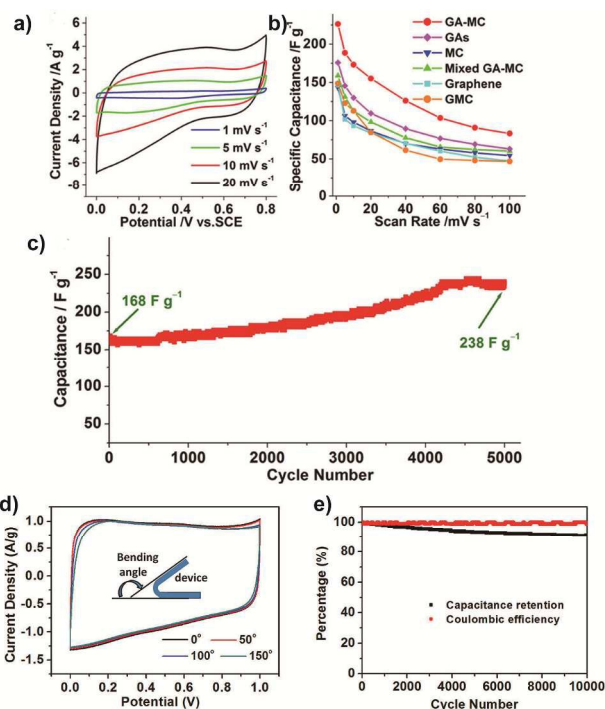


**Figure 5** The representative properties of supercapacitors using 3D graphene-based composites<sup>79,85</sup>

Wu, *et al.*<sup>79</sup> presented 3D graphene-based hierarchical macro- and meso-porous carbons (GA-MC) as super-capacitor electrodes. As shown in **Figure 5a**, the cyclic voltammetry profiles exhibit a typical electrical double layer behavior at all sweeping rates by virtue of a strong synergistic effect between macro- and mesopores. 3D GA-MC manifested outstanding specific capacitance of  $226 \text{ F}\cdot\text{g}^{-1}$  at  $1 \text{ mV}\cdot\text{s}^{-1}$ , which was much higher than those of the macroporous graphene, mesoporous carbon without involving graphene, physically mixed GA-MC with a 1:1 weight ratio, 2D graphene-based mesoporous carbon sheets without macropores, and reduced graphene powder (Figure 5b). There was no remarkable capacitance loss for GA-MC electrodes even after 5000 cycles (Figure 5c). The reason might be attributed to the improvement of ion accessibility in 3D graphene frameworks during the cycling process. Later, using 3D N and B co-doped monolithic graphene aerogels (BN-GAs), the group further initiated a simplified prototype of all-solid-state super-capacitors (ASSSs).<sup>80</sup> In the integrated electrode-separator-electrolyte prototype, GAs served as additive/binder-free electrodes and a

PVA/H<sub>2</sub>SO<sub>4</sub> gel as solid-state electrolyte and thinner separator, respectively. Owing to doping N and/or B in carbon networks, charge transfer was greatly facilitated between neighboring carbon atoms, with high specific capacitance ( $\sim 62 \text{ F}\cdot\text{g}^{-1}$ ) and enhanced energy density ( $\sim 8.65 \text{ W}\cdot\text{h}\cdot\text{kg}^{-1}$ ) and power density ( $\sim 1600 \text{ W}\cdot\text{kg}^{-1}$ ) comparing to the corresponding undoped, N doped or B doped GAs. Monolithic GAs materials would provide a potential for more efficient, light, minimized energy-storage devices.

By virtue of the reinforcing effect of PANI, Tai, *et al.*<sup>81</sup> developed a 3D graphene/polyaniline (GNS/PANI) composite hydrogel as supercapacitor electrodes. The as-prepared device exhibited a specific capacitance of  $334 \text{ F}\cdot\text{g}^{-1}$ , which is about 150% higher than that of pure GNS hydrogel-based electrode. GNS/PANI hydrogel might be a novel promising candidate for high-performance capacitor electrodes. Soon later, the same conclusion was effectively confirmed by Dong, *et al.*<sup>82</sup> Liu, *et al.*<sup>83</sup> and Liu, *et al.*<sup>84</sup>, respectively.

In 2013, Xu, *et al.*<sup>85</sup> reported a flexible solid-state supercapacitor using a  $120 \mu\text{m}$ -thick graphene hydrogel film as the electrode and PVA/H<sub>2</sub>SO<sub>4</sub> gel as the electrolyte (Figure 5d). The resulting device exhibited a high gravimetric specific capacitance of  $186 \text{ F/g}$  at  $1 \text{ A/g}$ , excellent rate capability of 70% retention at  $20 \text{ A/g}$ , a small leakage current of as little as  $10.6 \mu\text{A}$ , and an unprecedented area-specific capacitance of  $372 \text{ mF/cm}^2$ . Especially, at a current density of  $10 \text{ A/g}$ , only 8.4% capacitance decayed over 10000 charge/discharge cycles (Figure 5e). The reason may be attributed to the exceptionally mechanical and electrical robustness of the high interconnected network structure of graphene hydrogel films.

3D graphene networks have been confirmed to be an ideal supporter for active materials. From this point, He, *et al.*<sup>86</sup> reported a flexible super-capacitor using 3D graphene networks loaded with MnO<sub>2</sub> as electrodes. Under the optimized MnO<sub>2</sub> content, a maximum specific capacitance of  $130 \text{ F/g}$  and a high area capacitance of  $1.42 \text{ F/cm}^2$  at a scan rate of  $2 \text{ mV/s}$  were reached. Ji, *et al.*<sup>87</sup> and Wang, *et al.*<sup>88</sup> further described MnO<sub>2</sub>-wrapped graphene aerogels and graphene-VO<sub>2</sub> nanobelt hydrogels as super-capacitor electrodes, respectively. All the resultant hydrogels exhibited high specific capacitance, remarkable rate capability and excellent cycling ability.

Ye, *et al.*<sup>89</sup> utilized graphene aerogel-nickel foam as a binder-free super-capacitor electrode. The resulting electrode exhibited a high specific capacitance of  $366 \text{ F}\cdot\text{g}^{-1}$  at a current density of  $2 \text{ A}\cdot\text{g}^{-1}$  owing to the synergistic effect among the hierarchically porous structure, large specific surface area, high conductivity, low contact resistance, and sufficient deposition mass of graphene aerogel. Bello, *et al.*<sup>90</sup> reported the application of graphene foams decorated with silver nanoparticles in a three-electrode electrochemical cell. Soon later, binding bimetal to flexible graphene sheets, Xu, *et al.*<sup>91</sup> prepared a 3D graphene sandwiched structures with NiAl-layered double hydroxide nanosheets. The as-prepared electrode showed a specific capacitance of  $1329 \text{ F}\cdot\text{g}^{-1}$  at a current density of  $3.57 \text{ A}\cdot\text{g}^{-1}$  and at least 91% of the specific capacitance maintained after 500 cycles at  $15.3 \text{ A}\cdot\text{g}^{-1}$ . All these demonstrated that graphene foams were an excellent platform to incorporate metal particles for improving their electrochemical performance.

In order to obtain excellent desalination behavior during the capacitive deionization (CDI) process, Wang, *et al.*<sup>92</sup> opened up a novel opportunity to prepare high performance CDI electrodes utilizing 3D macroporous graphene architectures (3DMGA). The electro sorption capacity of the proposed 3DMGA electrode was *ca.* 3.9 mg·g<sup>-1</sup>, which was much higher than those of commercial activated carbon (2.9 mg·g<sup>-1</sup>) and 2D graphene in the literature (1.0~2.0 mg·g<sup>-1</sup>).<sup>93, 94</sup> 3DMGA are promising materials for high performance CDI electrodes. Using a 3D graphene-based hierarchically porous carbon as an electrode for CDI, Wen, *et al.*<sup>95</sup> drew the same conclusion as above.

Very recently, Li, *et al.*<sup>96</sup> further presented a KOH-activated 3D graphene as electrode materials for the CDI application. The resultant electrode possessed a super-large specific surface area of 3513m<sup>2</sup>/g, high electrical conductivity of 104S/m, and a high electroadsorption capacity of 11.86 mg NaCl/g C for 74 mg/L NaCl solution within 25 min. The superior electroadsorption capacity and the fast adsorption rate make KOH-activated 3D graphene an ideal electrode material for micro CDI in miniaturized water-cooling system.

Our group grew porous NiO nanoflakes on 3D graphene scaffolds and utilized them as monolithic free-standing electrodes for pseudo-supercapacitor without any other binders or metal-based current collectors.<sup>57</sup> The hierarchical NiO-3D graphene composite delivered a high specific capacity of ~1829 F·g<sup>-1</sup> at a current density of 3 A·g<sup>-1</sup> (the theoretical capacitance of NiO is 2584 F·g<sup>-1</sup>). A full-cell was realized with an energy density of 138 Wh·kg<sup>-1</sup> at a power density of 5.25 kW·kg<sup>-1</sup>, which is much superior than commercial ones as well as reported devices in asymmetric capacitors of NiO. Furthermore, the asymmetric super-capacitor exhibited capacitance retention of 85% after 5000 cycles relative to the initial value of the 1st cycle.

### 3.3 Solar cells and fuel cells

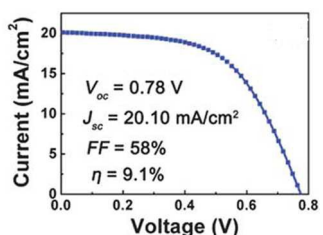


**Figure 6** The J-V characteristics of CdTe solar cell with 3D graphene back electrode<sup>97</sup>

Nowadays, environmental concerns and the finite nature of fossil fuels have led to great interest and fast development in the field of renewable energy sources. Solar energy conversion is one of the most promising ways to resolve this problem. Among all the methods to utilize solar energy, solar cells are a common electrical device that directly converts the energy of light into electricity by the photovoltaic effect. To investigate the application of 3D graphene composites in solar cells, Bi, *et al.*<sup>97</sup> prepared 3D graphene networks and utilized them as back electrodes of CdTe solar cells. As shown in **Figure 6**, the as-constructed CdTe solar cell possessed a short-circuit photocurrent density ( $J_{sc}$ ) of 20.1 mA·cm<sup>-2</sup>, an open-circuit voltage ( $V_{oc}$ ) of 0.78 V, a fill factor ( $FF$ ) of 58.0% and an overall power conversion efficiency ( $\eta$ ) of 9.1%. The  $\eta$  was much higher than

those of CdTe cells with RGO (6.50%), B-doped graphene (7.86%) and carbon nanotubes (7.0%) as back electrodes. The reason maybe result from the fact that 3D interconnected porous network can greatly improve the hole-collecting ability and reduce the barrier height to form a better back contact with the p-CdTe.

Further, Tang, *et al.*<sup>98</sup> added 3D graphene networks into the photo-anodes of dye sensitized solar cells to boost the photovoltaic performance. Under AM-1.5G light intensity, the resultant  $\eta$  with 3D graphene networks (1 wt %)-P25 photo-anode increased by 32.7% from 4.96% to 6.58% comparing to that of pure P25 photo-anode. Under the optimized quality of the added 3D graphene networks, the  $\eta$  could further increase to 6.87%. The continuous porous structures of 3D graphene networks could efficiently reduce inter-sheet junction contact resistance between the graphene sheets and make the sample a great channel for carrier transport besides enhancing dye absorption and prolonging electron lifetime.

Microbial fuel cells (MFC) are another important sustainable and green energy source that can convert chemical energy in organic wastes into electricity and integrate environmental bioremediation with power production. To enhance bacteria loading onto the electrode and to increase extracellular electron transfer efficiency between bacteria and electrodes, Yong, *et al.*<sup>99</sup> developed a macroporous and monolithic MFC anode with PANI hybridized 3D graphene. The 3D graphene/PANI electrode with large specific surface area could integrate with bacterial biofilms three-dimensionally and accept electrons through multiplexing and highly conductive pathways. The maximum power density obtained from the resultant MFC is ~768 mW/m<sup>2</sup>, which is about 4 times higher than that from the carbon cloth MFC (~158 mW/m<sup>2</sup>). This study provides a new dimension to MFC anode design as well as to the applications of 3D porous graphene networks.

### 3.4 Cocatalytic Activity

Cocatalysts, a kind of polynary catalysts, play a crucial role in many heterogeneous catalytic processes. Since the properties of cocatalysts are dependent not only on their components but also on their structures, the development of cocatalysts with 3D structures have opened up a new opportunity for enhanced the catalytic properties. Moreover, 3D cocatalysts are crucial and easy to achieve the optimized properties by tailoring their structures with high loadings.

For example, Hu, *et al.*<sup>100</sup> designed a novel cocatalyst system with ternary Pt/PdCu nanoboxes anchored onto 3D graphene sheets (Pt/PdCu/3DGF). The peak current density was 183 mA·cm<sup>-2</sup> for ethanol oxidation reaction on Pt/PdCu/3DGF electrode, which was 3, 4, and 6 times more than those on the Pt/C electrode (55 mA·cm<sup>-2</sup>), Pt/3DGF electrode (45 mA·cm<sup>-2</sup>) and PdCu/3DGF electrode (27 mA·cm<sup>-2</sup>), respectively. A more than 6-fold improvement in activity per unit mass of Pt over the commercial Pt/C catalyst (E-TEK 20%) was obtained for the Pt/PdCu/3DGF electrode based on the peak current density. The geometry-defined Pt/PdCu/3DGF will be an excellent cocatalyst for ethanol electro-oxidation in alkaline media with great potentials.

Maiyalagan, *et al.*<sup>101</sup> further reported a catalyst for methanol electro-oxidation in acidic media, *i.e.*, a 3D porous graphene

monolith decorated with Pt nanoparticles. Due to the 3D seamlessly interconnected porous structure, high surface area and excellent conductivity, the obtained 3D graphene composites possessed much improved catalytic activity for methanol oxidation comparing with the 3D carbon fibers scaffold. The peak current density of the forward anodic peaks with 3D-graphene was approximately  $1.6 \text{ mA}\cdot\text{cm}^{-2}$ , nearly two times the peak current density of the carbon fiber ( $0.8 \text{ mA}\cdot\text{cm}^{-2}$ ) and also more than that of commercial Pt/C catalyst ( $1.39 \text{ mA}\cdot\text{cm}^{-2}$ ).<sup>102</sup> All this further suggests that 3D-graphene plays a critical role in promoting methanol oxidation. The work could be excellently extended by decorating free-standing 3D graphene with other noble metal nanoparticles or alloys for various electro-catalysis applications. For example, with Cu nanoparticles deposited onto 3D graphene hydrogels, Wu, *et al.*<sup>103</sup> demonstrated their good catalytic performance for both the reduction of 4-nitrophenol and the photo degradation of methyl orange.

Employing GO and ammonium thiocyanate as precursors, Su, *et al.*<sup>104</sup> developed 3D N and S co-doped graphene frameworks (N/S-GFs) as a metal-free catalyst to accelerate oxygen reduction reaction in alkaline condition. N/S-GFs showed a kinetic-limiting current density of  $3.90 \text{ mA}/\text{cm}^2$ , which was comparable to that of commercial Pt/C catalyst ( $4.2 \text{ mA}/\text{cm}^2$ ) and was much higher than  $2.8 \text{ mA}/\text{cm}^2$  for N-GFs measured at  $\sim 0.36 \text{ V}$ .

Recently, Chen, *et al.*<sup>105</sup> reported a 3D graphene-MnO<sub>2</sub> framework incorporated with NiCo<sub>2</sub>O<sub>4</sub> (G-Mn-NiCo). The resultant 3D porous G-Mn-NiCo presented an outstanding catalytic activity for electro-catalytic oxygen evolution with a more negative onset potential of 321 mV than other catalytic samples (366 mV for G-NiCo, 475 mV for 2DG-Mn-NiCo, 366 mV for G-Mn, 399 mV for graphene and 365 mV for NiCo), respectively. As the edges and defects of NiCo<sub>2</sub>O<sub>4</sub> were all active centers to expedite water dissociation, graphene-MnO<sub>2</sub> in the polynary coanalyst could significantly increase the use of NiCo<sub>2</sub>O<sub>4</sub> active species. For example, O atoms in MnO<sub>2</sub> or functional groups of graphene had low electronegativity, they might interact with Ni or Co atoms of NiCo<sub>2</sub>O<sub>4</sub> to form strong metal-O bonds. Moreover, Ni(Co)-O bonds were another active centers to boost water oxidation. Thus, a dual-active-site mechanism will be responsible for the great catalytic performance of G-Mn-NiCo.

### 3.5 Thermal Interface Material

Low operation temperature and efficient heat dissipation are quite important for device life in current photonic and electronic technologies. However, high interfacial thermal resistance between contact solid surfaces resulted in a major bottleneck of heat dissipation in various devices. 3D graphene-based porous structures may be a novel promising candidate for thermal interfacial materials (TIMs) by both theoretical and experimental investigations owing to its high thermal conductivity, the large surface-to-volume ratio and continuously covalent-bond porous networks. For example, Liang, *et al.*<sup>106</sup> constructed 3D vertically aligned multilayer graphene sheets TIM (VA-fMG TIM) between silicon/silicon surfaces using pure indium as a metallic medium. The target composites VA-fMG possessed an excellent thermal conductivity of  $\sim 112 \text{ W}\cdot\text{m}^{-1}\cdot\text{K}^{-1}$  at 25 °C and an ultralow thermal expansion coefficient of  $\sim -0.71 \text{ ppm}\cdot\text{K}^{-1}$  in the in-plane direction without any reduction process. Compared with their

counterpart of recumbent aligned multilayer graphene sheets between silicon surfaces, VA-fMG TIM had a significantly higher equivalent thermal conductivity of  $75.5 \text{ W}\cdot\text{m}^{-1}\cdot\text{K}^{-1}$  and a lower contact thermal resistance of  $5.1 \text{ mm}^2\cdot\text{K}\cdot\text{W}^{-1}$ . This finding will provide a throughout approach for a graphene-based TIM assembly as well as knowledge of vertically aligned graphene architectures.

Pettes, *et al.*<sup>107</sup> prepared 3D freestanding GFs comprised of few layer graphene and ultrathin graphite and studied their thermal properties in detail. The room-temperature thermal conductivity ( $\kappa_{\text{GF}}$ ) of the resultant GF, with a solid concentration of *ca.*  $0.45\pm 0.09 \text{ vol } \%$ , was increased from 0.26 to  $1.7 \text{ W}\cdot\text{m}^{-1}\cdot\text{K}^{-1}$  when the etchants for the sacrificial nickel supports changed from an aggressive hydrochloric acid to a slow ammonium persulfate. The  $\kappa_{\text{GF}}$  showed a quadratic dependence on temperature between 11 and 75 K and peaked at *ca.* 150 K, eliminating internal contact thermal resistance in the continuous GF structure. 3D graphene-based architecture would be a promising thermal interface and heat spreading material.

Ahn, *et al.*<sup>108</sup> reported a novel boiling heat transfer phenomenon using RGO colloid. A 3D interconnected foam-like graphene multilayer will be self-assembled on the heater surface once the RGO colloid boiled. This phenomenon would provide an efficient and safe boiling heat transfer mode to eliminate the sudden and rapid increase of wall temperature at critical heat flux, a dangerous limitation of nucleate boiling heat transfer.

Recently, Zhang, *et al.*<sup>109</sup> uncovered the thermal interface properties of GF, too. The thermal interfacial resistance of GF at Si-Al interface was as low as  $0.04 \text{ cm}^2\cdot\text{K}\cdot\text{W}^{-1}$ , which outperformed the commercially available thermal grease and pastes, and had an enhancement of at least  $\sim 75\%$  to that of the best reported among carbon-based TIMs.<sup>110-112</sup> The thermal contact resistance between GF and the mating surface accounted for the major part of all the overall thermal resistance, with an asymptotic-type conformation and a plateau value at an ultralow contact pressure ( $\sim 0.1 \text{ MPa}$ ). 3D GF could conform well to the mating surface and fill in the gaps between the mating surfaces, so it could serve as next generation high performance TIM for thermal management in electronic packages.

### 3.6 Sensors

3D porous graphene nanostructures have great advantages for applying as an excellent sensing platform due to the strong synergistic effects between graphene and the chromophores, besides its large 3D active surface area which maximizes exposure to analytes. Charge carriers can also move rapidly with a little resistance through the continuous and interconnected graphene networks and so boost analytic sensitivity.

Combining 3D graphene porous structure with 1-butyl-3-methylimidazolium hexafluorophosphate ionic liquid, Ng, *et al.*<sup>113</sup> reported a novel carbon paste electrode for amperometric detection of NO. The NO oxidation in the presence of the resultant composite possessed a fast response of less than 4 seconds, an excellent sensitivity of  $11.2 \text{ mA}\cdot\text{cm}^{-2}(\text{mmol/L})^{-1}$  and an extremely low detection limit of 16 nM, which were all superior to those of all relevant reported works based on carbon nanotubes and nanoparticles.<sup>114, 115</sup> The results demonstrate that the 3D graphene/ionic liquid composites can provide a sensitive NO detection and further a robust electrode material in various

electrochemical devices.

Yavari, *et al.*<sup>116</sup> reported a foam-like 3D graphene network, which efficiently merged the merits of both nanostructures and conducting-polymer. Based on the changes in their electrical conductivity, the proposed sensor to detect NH<sub>3</sub> and NO<sub>2</sub> possessed a highly sensitivity of parts-per-million level detection limit in air at room-temperature. Especially, only through Joule-heating, all the chemisorbed molecules could be expelled from the foam's surface leading to full-reversibility. This work provides a promising thought for reversibly determining, enriching and separating air pollutions.

Using 3D graphene as a template to anchor some electro-active materials, *i.e.* Pt nanoparticles and multiwalled carbon nanotubes, Cao, *et al.*<sup>71</sup> for the first time, developed them as electrochemical sensors to detect H<sub>2</sub>O<sub>2</sub>. The detection limit was as low as 8.6 nM. 3D porous graphene networks would be a novel and promising platform to anchor other electro-active materials for electrochemical sensors. Later, 3D GFs incorporating Pt-Ru bimetallic nanoparticles (PtRu/3DGF) was developed by Kung, *et al.*<sup>117</sup> for detecting H<sub>2</sub>O<sub>2</sub>. PtRu/3DGF exhibited an excellent catalytic activity toward electrochemical oxidation of H<sub>2</sub>O<sub>2</sub> without any additional mediator, showing a high sensitivity (1023.1 mA·mM<sup>-1</sup>·cm<sup>-2</sup>) and a low detection limit (0.04 mM). Yuan, *et al.*<sup>118</sup> reported 3D graphene hydrogel decorated with PdCu bimetallic nanoparticles (PdCu/GE) to detect glucose in the alkaline solution containing chloride ions. At -0.4 V, the PdCu/GE modified electrode presented quick respond to glucose oxidation with a wide linear range from 1mM to 18 mM and a reproducible sensitivity of 48 μA(mg·mM)<sup>-1</sup>.

Yang, *et al.*<sup>119</sup> constructed a flexible 3D graphene network-based chemical sensor deposited on paper substrate. After 3D graphene foam network was transferred to a flexible and environment-friendly paper substrate, a sensing electrode was established. The resulting 3D graphene foam-based sensor on a paper substrate was very reliable with sensitivity up to 200 ppm and 800 ppm, respectively, when either compressive (-0.5%) or tensile (+0.5%) strain was applied with introducing NO<sub>2</sub> gas. After each experiment, the sensors could be refreshed by UV treatment in a vacuum condition, which assured the lowest baseline by accelerating the desorption process.

Yang, *et al.*<sup>120</sup> prepared large-area 3D graphene intercalated by PANI nanofibers and investigated it to determine guanine and adenine. Because of the negative charge and the specific structure, the resultant composite could prompt adsorbing positively charged guanine and adenine via strong π-π\* interactions or electrostatic adsorption. Under the optimized conditions, the anodic peak currents to detect guanine and adenine were linear over a large range of 0.5 to 200 μmol·L<sup>-1</sup> with the detection limits of 7.5×10<sup>-8</sup> and 5.0×10<sup>-8</sup> mol·L<sup>-1</sup> for guanine and adenine, respectively. In the related physiological process, the developed sensing platform would be used to determinate other small molecules.

Another 3D graphene incorporated with polydimethyl-siloxane micropillars was constructed for sensitively enzyme-based phenol detection.<sup>121</sup> Using the proposed 3D graphene-based composite as a working electrode, an excellent electron-transfer property was demonstrated in 1 mM K<sub>3</sub>Fe(CN)<sub>6</sub> and 0.1 M KCl solution. After tyrosinase enzymes were immobilized on the surface of the

graphene micropillar, it was effective to detect phenol in the microchannel with a detection limit of 50 nM. This is the first demonstration of using 3D graphene as an excellent electrochemical biosensor in the microfluidic system.

Xi, *et al.*<sup>122</sup> developed another 3D non-enzymatic electrochemical sensor for sensitively detecting H<sub>2</sub>O<sub>2</sub>. Using in-situ polymerized polydopamine as the linker, the 3D graphene-based electrode was functionalized with thionine molecules to mediate the reduction of H<sub>2</sub>O<sub>2</sub> at close proximity to the electrode surface. Such a sensor could detect H<sub>2</sub>O<sub>2</sub> with a wide linear range (0.4 to 660 μM), high sensitivity (169.7 μA mM<sup>-1</sup>), low detection limit (80 nM), and fast response (reaching 95% of the steady current within 3 s). Furthermore, this sensor was efficiently used for real-time detection of dynamic release of H<sub>2</sub>O<sub>2</sub> from live cancer cells in response to a pro-inflammatory stimulant.

### 3.7 Enrichment and Separation

Owing to the global scale of severe water and air contaminations arising from industrial/agricultural pollutants and oil spills, the development of novel strategies to separate and absorb air and water contaminants should be of significant importance for environmental issues.<sup>19</sup> However, to produce functional materials with high absorbency and excellent recyclability and tolerance under harsh conditions still remains a key challenge for practical applications. 3D graphene porous nano networks have attracted a great deal of research interest because of their intriguing properties such as superior chemical stability, large surface-to-volume ratio, excellent electrical conductivities, and high thermal and mechanical stability, *etc.*

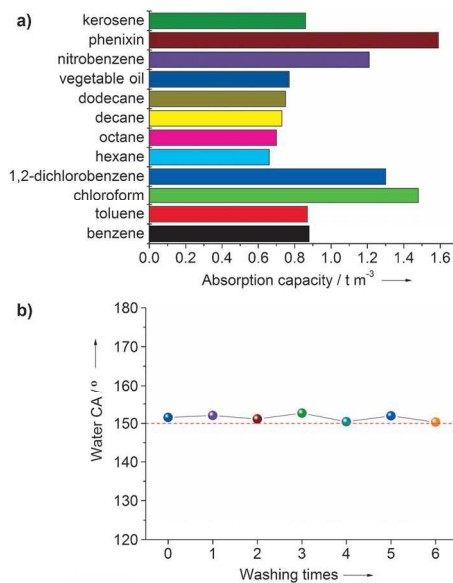


**Figure 7** (a) Theoretical absorption capacities of 3D-SMF for different organic compounds and oils. (b) Relationship between washing times and water CA of the SMF<sup>125</sup>

The sorption abilities of 3D graphene networks to N<sub>2</sub>, H<sub>2</sub>, CO<sub>2</sub> and water vapor were investigated and reported by Wang, *et al.*<sup>123</sup> 3D graphene materials, with a mesoporosity centered at 4 nm and a specific surface area of *ca.* 477 m<sup>2</sup>/g, possessed quite high absorbencies to the gases above. For example, the H<sub>2</sub> sorption capacities were 1.40 and 1.25% by weight at 77 and 87 K under

106.6 kPa, respectively. The CO<sub>2</sub> sorption capacity was 2.98% by weight at 273 K under 106.6 kPa and the water vapor sorption capacity was 18.7% by weight at 293 K under 97.0 kPa. All the data could be used for characterization and molecular simulation of adsorption/diffusion in carbonaceous adsorbents.

As water pollutant adsorbents, Liu, *et al.*<sup>124</sup> demonstrated the potential of 3D GO sponges to remove both methylene blue (MB) and methyl violet (MV) dyes, two main contaminants from the dye manufacturing and textile finishing. The results showed that 99.1% of MB and 98.8% of MV could be removed and the equilibrium status could reach within 2 min. 3D GO sponges displayed an excellent adsorption capacity as high as 397 and 467 mg·g<sup>-1</sup> for MB and MV dye, respectively. The adsorption mechanism for MB and MV may be attributed to the endothermic chemical adsorption through the strong  $\pi$ - $\pi$  stacking and anion-cation interaction with the activation energy of 50.3 and 70.9 kJ mol<sup>-1</sup>, respectively. 3D GO sponges possess a high capability as a promising organic dye scavenger with a good efficiency.

Utilizing 3D graphene super-wetting mesh film (3D-SMF) prepared by a simple dip-coating method, Sun, *et al.*<sup>125</sup> developed a new strategy for selectively separating and absorbing organic compounds or oils from polluted water. As shown in Figure 7a, 3D-SMF possessed higher volume absorption capacities for a wide range of organic compounds and oils than that of any bulk absorbent materials reported by then.<sup>126-130</sup> Importantly, 3D-SMF can be regenerated simply by washing out the organic compounds or oils attached on the surface of the 3D-SMF after use and remained nearly unchanged after six cycles of absorption/washing test (Figure 7b). It means that 3D-SMF would be an ideal absorbent material for removing organic compounds or oils from polluted water on a large scale. 3D-SMF opens a prospective insight in liquid-liquid separation or selective absorption technology.

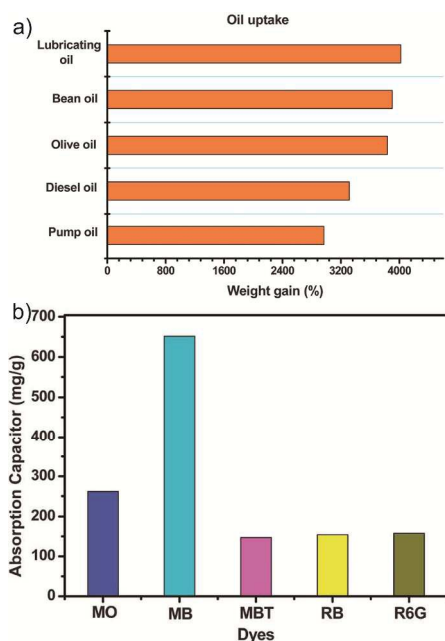


Figure 8 (a) The absorption capacities (saturated) of different oils by GAs, and (b) the absorption capacities of GAs for different dyes after 5 days<sup>103</sup>

Wu, *et al.*<sup>103</sup> fabricated porous graphene-based aerogels (GAs) and studied their absorption performances for different oils and organic dyes. As shown in Figure 8a, the absorption capacities were 28 to 40 times the weight of the GAs for the different oils related to the density of the oils. The absorption capacities of GAs for the different organic dyes ranged from 150 mg·g<sup>-1</sup> to 650 mg·g<sup>-1</sup> (Figure 8b). These results further confirm that GAs would be promising absorbents for removing dye or oil pollutants from contaminated water.

### 3.7 Others

Some other potential applications were also investigated apart from the major application fields mentioned above. For instance, Wang, *et al.*<sup>131</sup> prepared 3D graphene networks doped with different amount of Ni-B nanoalloys for hydrogen storage. 3D graphene with 0.83 wt% Ni and 1.09 wt% B showed a maximal reversible hydrogen storage capacity of 4.4 wt%, which was three times better than that of pristine graphene reported. The analysis of BET specific surface area and pore volume confirmed that the high hydrogen adsorption capacity comes from a process other than physical adsorption. To dope appropriate contents of Ni-B nanoalloys can lead to the dissociative chemisorption of hydrogen molecules by spillover to achieve a high hydrogen storage capacity.

Yu, *et al.*<sup>132</sup> demonstrated that 3D stacked multilayer graphene (s-MLG) for a potential candidate of interconnect applications. Compared with 3D exfoliated multilayer graphene, s-MLG possessed superior conduction due to the interlayer decoupling. The wire resistivity of s-MLG was continually reduced with increasing layers, while the contact resistance would be saturated with more stacked layer numbers. Therefore, the s-MLG system offers a promising material platform for high performance on-chip interconnect applications in the future.

Kim, *et al.*<sup>133</sup> efficiently demonstrated 3D GF-based transparent conductive electrodes for GaN-based blue light-emitting diodes (LEDs). After 3D GFs grown on 3D Cu foam were transferred onto a p-GaN layer of blue LEDs, their optical and electrical performances would be enhanced greatly. For example, at an injection current of 100 mA, the forward operating voltage and the light output power were improved by ~26% and ~14%, respectively. The robustness, high transmittance, and outstanding conductivity make 3D GFs great potentials for advanced transparent conductive electrodes in LED devices.

Due to their specific topographical, chemical and electrical properties, 3D GFs could be a promising candidate for novel tissue scaffold in the field of tissue engineering. Li, *et al.*<sup>134</sup> for the first time, utilized 3D porous GFs as a scaffold for neural stem cells (NSCs) in vitro. The result confirmed that 3D GFs could support NSCs growth, and also kept cells at a more active proliferation state with up regulation of Ki67 expression than that of 2D graphene films. The study implies the great potential of 3D GFs in NSC research, neural tissue engineering and neural prostheses, and so on.

## 4. Conclusions

3D graphene, as a vital platform to construct porous functional composites, has been at the center stage of research recently from both fundamental and technological viewpoints. A wide range of

3D graphene-based nano composites have been constructed and reported in recent reports through in situ reduction-assembly method, chemical vapor deposition, cross-linking method and template-direction methods. By virtue of their highly conductivity, robustly mechanical intensity, low mass density, high specific surface area, good compatibility and excellent flexibility, 3D graphene porous composites with interconnected networks have been widely applied in lithium-ion batteries, super-capacitors, solar cells and fuel cells, co-catalysts, chemical sensors, contamination absorbents and even biomimetic composites with excellent performances and potentials. It is expected that with the research effort of all us, the engineering and applications of 3D graphene-based porous nano composites will have a much greater and better future either in all of the above-mentioned fields or in other novel applications not envisaged.

## Acknowledgements

The authors gratefully acknowledge the financial supports from the National Natural Science Fund of China (Nos: 21277103 and 21271141), Anhui Provincial Natural Science Fund (No: 1508085QB35) and Science and Technology Project of Anhui Province (Nos: 1206c0805031 and 1406c085021).

## Notes and references

<sup>a</sup>Anhui Provincial Laboratory of Biomimetic Sensor and Detecting Technology & Solar Photovoltaic Materials Research Center, West Anhui University, Lu'an 237012, China, E-mail: [yanzhq2008@163.com](mailto:yanzhq2008@163.com)

<sup>b</sup>Jiangxi Research Institute of Tungsten and Rare Earths & School of Materials and Chemical Engineering, Jiangxi University of Science and Technology, Ganzhou, 341000, China

<sup>c</sup>Center of Super-Diamond and Advanced Films (COSDAF) & Dept. of Phys. and Mater. Sci., City University of Hong Kong, Hong Kong, E-mail: [apcslee@cityu.edu.hk](mailto:apcslee@cityu.edu.hk)

† Electronic Supplementary Information (ESI) available: [details of any supplementary information available should be included here]. See DOI: 10.1039/b000000x/

- K. S. Novoselov, A. K. Geim, S. V. Morozov, D. Jiang, Y. Zhang, S. V. Dubonos, I. V. Grigorieva and A. A. Firsov, *Science*, 2004, **306**, 666-669.
- J. G. Ren, C. D. Wang, Q. H. Wu, X. Liu, Y. Yang, L. F. He and W. J. Zhang, *Nanoscale*, 2014, **6**, 3353-3360.
- Z. Y. Yin, J. X. Zhu, Q. Y. He, X. H. Cao, C. L. Tan, H. Y. Chen, Q. Y. Yan and H. Zhang, *Adv Energy Mater*, 2014, **4**, 1300574.
- L. Chen, Y. Zhou, W. G. Tu, Z. D. Li, C. X. Bao, H. Dai, T. Yu, J. G. Liu and Z. G. Zou, *Nanoscale*, 2013, **5**, 3481-3485.
- S. AbdulAlmohsin and J. B. Cui, *J Phys Chem C*, 2012, **116**, 9433-9438.
- H. B. Yang, G. H. Guai, C. X. Guo, Q. L. Song, S. P. Jiang, Y. L. Wang, W. Zhang and C. M. Li, *J Phys Chem C*, 2011, **115**, 12209-12215.
- G. Kalita, M. Matsushima, H. Uchida, K. Wakita and M. Umeno, *J Mater Chem*, 2010, **20**, 9713-9717.
- X. M. Li, D. Xie, H. Park, T. H. Zeng, K. L. Wang, J. Q. Wei, M. L. Zhong, D. H. Wu, J. Kong and H. W. Zhu, *Adv Energy Mater*, 2013, **3**, 1029-1034.
- D. D. Nguyen, N. H. Tai, S. Y. Chen and Y. L. Chueh, *Nanoscale*, 2012, **4**, 632-638.
- H. A. Becerril, J. Mao, Z. Liu, R. M. Stoltenberg, Z. Bao and Y. Chen, *ACS Nano*, 2008, **2**, 463-470.
- S. Watcharotone, D. A. Dikin, S. Stankovich, R. Piner, I. Jung, G. H. B. Dommett, G. Evmenenko, S. E. Wu, S. F. Chen, C. P. Liu, S. T. Nguyen and R. S. Ruoff, *Nano Lett*, 2007, **7**, 1888-1892.
- S. Roche, *Nat Nanotechnol*, 2011, **6**, 8-9.
- M. Freitag, *Nat Nanotechnol*, 2008, **3**, 455-457.
- R. M. Westervelt, *Science*, 2008, **320**, 324-325.
- V. C. Tung, L. M. Chen, M. J. Allen, J. K. Wassei, K. Nelson, R. B. Kaner and Y. Yang, *Nano Lett*, 2009, **9**, 1949-1955.
- X. Li, C. Y. Li, H. W. Zhu, K. L. Wang, J. Q. Wei, X. M. Li, E. Y. Xu, Z. Li, S. Luo, Y. Lei and D. H. Wu, *Chem Commun*, 2010, **46**, 3502-3504.
- G. W. Xu, J. W. Liu, Q. Wang, R. Q. Hui, Z. J. Chen, V. A. Maroni and J. Wu, *Adv Mater*, 2012, **24**, Op71-Op76.
- X. C. Dong, W. Huang and P. Chen, *Nanoscale Res Lett*, 2011, **6**, 60.
- Z. Q. Yan, H. T. Xue, K. Berning, Y.-W. Lam and C.-S. Lee, *ACS Appl Mater Interfaces*, 2014, **6**, 22761-22768.
- F. Yang, M. W. Xu, S. J. Bao and H. Wei, *RSC Adv*, 2013, **3**, 25317-25322.
- W. F. Chen and L. F. Yan, *Nanoscale*, 2011, **3**, 3132-3137.
- G. H. Moon, Y. Shin, D. Choi, B. W. Arey, G. J. Exarhos, C. Wang, W. Choi and J. Liu, *Nanoscale*, 2013, **5**, 6291-6296.
- Y. J. Wang, F. M. Wang and J. He, *Nanoscale*, 2013, **5**, 11291-11297.
- J. S. Lee, H. J. Ahn, J. C. Yoon and J. H. Jang, *Phys Chem Chem Phys*, 2012, **14**, 7938-7943.
- M. Zeng, W. L. Wang and X. D. Bai, *Chin Phys B*, 2013, **22**, 098105.
- M. A. Worsley, P. J. Pauzauksie, T. Y. Olson, J. Biener, J. H. Satcher and T. F. Baumann, *J Am Chem Soc*, 2010, **132**, 14067-14069.
- P. Si, S. J. Ding, X. W. Lou and D. H. Kim, *RSC Adv*, 2011, **1**, 1271-1278.
- G. Y. Zhu, Z. He, J. Chen, J. Zhao, X. M. Feng, Y. W. Ma, Q. L. Fan, L. H. Wang and W. Huang, *Nanoscale*, 2014, **6**, 1079-1085.
- S. Park, S. O. Kang, E. Jung, S. Park and H. S. Park, *RSC Adv*, 2014, **4**, 899-902.
- M. M. Gao, C. K. N. Peh, W. L. Ong and G. W. Ho, *RSC Adv*, 2013, **3**, 13169-13177.
- F. He, N. Niu, F. Y. Qu, S. Q. Wei, Y. J. Chen, S. L. Gai, P. Gao, Y. Wang and P. Yang, *Nanoscale*, 2013, **5**, 8507-8516.
- Z. Han, Z. H. Tang, P. Li, G. Z. Yang, Q. B. Zheng and J. H. Yang, *Nanoscale*, 2013, **5**, 5462-5467.
- X. C. Dong, Y. F. Cao, J. Wang, M. B. Chan-Park, L. H. Wang, W. Huang and P. Chen, *RSC Adv*, 2012, **2**, 4364-4369.
- S. M. Avdoshenko, C. G. da Rocha and G. Cuniberti, *Nanoscale*, 2012, **4**, 3168-3174.
- C. Li and G. Q. Shi, *Nanoscale*, 2012, **4**, 5549-5563.
- S. Nardecchia, D. Carriazo, M. L. Ferrer, M. C. Gutierrez and F. del Monte, *Chem Soc Rev*, 2013, **42**, 794-830.
- H. C. Gao and H. W. Duan, *Biosens Bioelectron*, 2015, **65**, 404-419.
- Z. Q. Yan, S. Y. Guang, H. Y. Xu and X. Y. Liu, *Dyes Pigm*, 2013, **99**, 720-726.
- Z. Q. Yan, S. Y. Guang, H. Y. Xu, X. Y. Su, X. L. Ji and X. Y. Liu, *RSC Adv*, 2013, **3**, 8021-8027.
- L. Hu, Z. Q. Yan and H. Y. Xu, *RSC Adv*, 2013, **3**, 7667-7676.

41. J. L. Vickery, A. J. Patil and S. Mann, *Adv Mater*, 2009, **21**, 2180-2184.
42. S. H. Lee, H. W. Kim, J. O. Hwang, W. J. Lee, J. Kwon, C. W. Bielawski, R. S. Ruoff and S. O. Kim, *Angew Chem, Int Ed*, 2010, **49**, 10084-10088.
43. H. J. Jo, H. Noh, M. Kaviani, J. M. Kim, M. H. Kim and H. S. Ahn, *Carbon*, 2015, **81**, 357-366.
44. Z. H. Tang, S. L. Shen, J. Zhuang and X. Wang, *Angew Chem, Int Ed*, 2010, **49**, 4603-4607.
45. W. Lv, Y. Tao, W. Ni, Z. Zhou, F. Y. Su, X. C. Chen, F. M. Jin and Q. H. Yang, *J Mater Chem*, 2011, **21**, 12352-12357.
46. Y. X. Xu, Q. O. Wu, Y. Q. Sun, H. Bai and G. Q. Shi, *ACS Nano*, 2010, **4**, 7358-7362.
47. X. Jiang, Y. W. Ma, J. J. Li, Q. L. Fan and W. Huang, *J Phys Chem C*, 2010, **114**, 22462-22465.
48. M. A. Worsley, T. Y. Olson, J. R. I. Lee, T. M. Willey, M. H. Nielsen, S. K. Roberts, P. J. Pauzuskie, J. Biener, J. H. Satcher and T. F. Baumann, *J Phys Chem Lett*, 2011, **2**, 921-925.
49. K. W. Chen, L. B. Chen, Y. Q. Chen, H. Bai and L. Li, *J Mater Chem*, 2012, **22**, 20968-20976.
50. J. L. Wang, Z. X. Shi, J. C. Fan, Y. Ge, J. Yin and G. X. Hu, *J Mater Chem*, 2012, **22**, 22459-22466.
51. C. Wu, X. Y. Huang, G. L. Wang, L. B. Lv, G. Chen, G. Y. Li and P. K. Jiang, *Adv Funct Mater*, 2013, **23**, 506-513.
52. J. R. Potts, D. R. Dreyer, C. W. Bielawski and R. S. Ruoff, *Polymer*, 2011, **52**, 5-25.
53. C. G. Hu, X. Q. Zhai, L. L. Liu, Y. Zhao, L. Jiang and L. T. Qu, *Sci Rep*, 2013, **3**, 2065.
54. Z. P. Chen, W. C. Ren, L. B. Gao, B. L. Liu, S. F. Pei and H. M. Cheng, *Nature Mater*, 2011, **10**, 424-428.
55. S. Stankovich, D. A. Dikin, G. H. Dommett, K. M. Kohlhaas, E. J. Zimney, E. A. Stach, R. D. Piner, S. T. Nguyen and R. S. Ruoff, *Nature*, 2006, **442**, 282-286.
56. V. Sridhar, I. Lee, H. S. Yoon, H. H. Chun and H. Park, *Carbon*, 2013, **61**, 633-639.
57. C. D. Wang, J. L. Xu, M.-F. Yuen, J. Zhang, Y. Yangyang, X. F. Chen and W. J. Zhang, *Adv Funct Mater*, 2014, **24**, 6372-6380.
58. J. C. Yoon, J. S. Lee, S. I. Kim, K. H. Kim and J. H. Jang, *Sci Rep*, 2013, **3**, 1788.
59. X. Y. Xiao, T. E. Beechem, M. T. Brumbach, T. N. Lambert, D. J. Davis, J. R. Michael, C. M. Washburn, J. Wang, S. M. Brozik, D. R. Wheeler, D. B. Burckel and R. Polsky, *ACS Nano*, 2012, **6**, 3573-3579.
60. J. Li, T. F. Chung, Y. P. Chen and G. J. Cheng, *Nano Lett*, 2012, **12**, 4577-4583.
61. X. Xie, Y. L. Zhou, H. C. Bi, K. B. Yin, S. Wan and L. T. Sun, *Sci Rep*, 2013, **3**, 2117.
62. Y. Zhu, L. Li, C. G. Zhang, G. Casillas, Z. Z. Sun, Z. Yan, G. D. Ruan, Z. W. Peng, A. R. O. Raji, C. Kittrell, R. H. Hauge and J. M. Tour, *Nature Commun*, 2012, **3**, 1225.
63. V. Sridhar, H. J. Kim, J. H. Jung, C. Lee, S. Park and I. K. Oh, *ACS Nano*, 2012, **6**, 10562-10570.
64. B. You, L. L. Wang, L. Yao and J. Yang, *Chem Commun*, 2013, **49**, 5016-5018.
65. Y. Y. Li, Z. S. Li and P. K. Shen, *Adv Mater*, 2013, **25**, 2474-2480.
66. Y. Liu, Y. Ma, S. Y. Guang, F. Y. Ke and H. Y. Xu, *Carbon*, 2015, **83**, 79-89.
67. Y. F. Tang, F. Q. Huang, H. Bi, Z. Q. Liu and D. Y. Wan, *J Power Sources*, 2012, **203**, 130-134.
68. Y. H. Ding, H. M. Ren, Y. Y. Huang, F. H. Chang and P. Zhang, *Mater Res Bull*, 2013, **48**, 3713-3716.
69. P. L. Kuo, C. H. Hsu, H. T. Chiang and J. M. Hsu, *J Nanopart Res*, 2013, **15**(12): 1-8.
70. S. X. Yu, L. W. Yang, Y. Tian, P. Yang, F. Jiang, S. W. Hu, X. L. Wei and J. X. Zhong, *J Mater Chem A*, 2013, **1**, 12750-12758.
71. X. H. Cao, Z. Y. Zeng, W. H. Shi, P. R. Yep, Q. Y. Yan and H. Zhang, *Small*, 2013, **9**, 1703-1707.
72. J. S. Luo, J. L. Liu, Z. Y. Zeng, C. F. Ng, L. J. Ma, H. Zhang, J. Y. Lin, Z. X. Shen and H. J. Fan, *Nano Lett*, 2013, **13**, 6136-6143.
73. R. J. Chen, T. Zhao, J. Lu, F. Wu, L. Li, J. Z. Chen, G. Q. Tan, Y. S. Ye and K. Amine, *Nano Lett*, 2013, **13**, 4642-4649.
74. Y. Yang, M. T. McDowell, A. Jackson, J. J. Cha, S. S. Hong and Y. Cui, *Nano Lett.*, 2010, **10**, 1486-1491.
75. J. C. Ye, S. Chamvanichborikam, M. A. Worsley, S. O. Kucheyev, B. C. Wood and Y. M. Wang, *Carbon*, 2015, **85**, 269-278.
76. C. D. Wang, Y. Li, Y. S. Chui, Q. H. Wu, X. F. Chen and W. J. Zhang, *Nanoscale*, 2013, **5**, 10599-10604.
77. Z. J. Fan, J. Yan, L. J. Zhi, Q. Zhang, T. Wei, J. Feng, M. L. Zhang, W. Z. Qian and F. Wei, *Adv Mater*, 2010, **22**, 3723-3728.
78. Z. Yan, L. L. Ma, Y. Zhu, I. Lahiri, M. G. Hahm, Z. Liu, S. B. Yang, C. S. Xiang, W. Lu, Z. W. Peng, Z. Z. Sun, C. Kittrell, J. Lou, W. B. Choi, P. M. Ajayan and J. M. Tour, *ACS Nano*, 2013, **7**, 58-64.
79. Z. S. Wu, Y. Sun, Y. Z. Tan, S. B. Yang, X. L. Feng and K. Mullen, *J Am Chem Soc*, 2012, **134**, 19532-19535.
80. Z. S. Wu, A. Winter, L. Chen, Y. Sun, A. Turchanin, X. L. Feng and K. Mullen, *Adv Mater*, 2012, **24**, 5130-5135.
81. Z. X. Tai, X. B. Yan and Q. J. Xue, *J Electrochem Soc*, 2012, **159**, A1702-A1709.
82. X. C. Dong, J. X. Wang, J. Wang, M. B. Chan-Park, X. G. Li, L. H. Wang, W. Huang and P. Chen, *Mater Chem Phys*, 2012, **134**, 576-580.
83. H. L. Liu, Y. Wang, X. L. Gou, T. Qi, J. Yang and Y. L. Ding, *Mat Sci Eng B-Solid*, 2013, **178**, 293-298.
84. Y. Liu, Y. Ma, S. Y. Guang, H. Y. Xu and X. Y. Su, *J Mater Chem A*, 2014, **2**, 813-823.
85. Y. X. Xu, Z. Y. Lin, X. Q. Huang, Y. Liu, Y. Huang and X. F. Duan, *ACS Nano*, 2013, **7**, 4042-4049.
86. Y. M. He, W. J. Chen, X. D. Li, Z. X. Zhang, J. C. Fu, C. H. Zhao and E. Q. Xie, *ACS Nano*, 2013, **7**, 174-182.
87. C. C. Ji, M. W. Xu, S. J. Bao, Z. J. Lu, C. J. Cai, H. Chai, R. Y. Wang, F. Yang and H. Wei, *New J Chem*, 2013, **37**, 4199-4205.
88. H. W. Wang, H. Yi, X. Chen and X. F. Wang, *Journal of Materials Chemistry A*, 2014, **2**, 1165-1173.
89. S. B. Ye, J. C. Feng and P. Y. Wu, *ACS Appl Mater Interfaces*, 2013, **5**, 7122-7129.
90. A. Bello, M. Fabiane, D. Dodoo-Arhin, K. I. Ozoemena and N. Manyala, *J Phys Chem Solids*, 2014, **75**, 109-114.
91. J. Xu, S. L. Gai, F. He, N. Niu, P. Gao, Y. J. Chen and P. P. Yang, *J Mater Chem A*, 2014, **2**, 1022-1031.
92. H. Wang, D. S. Zhang, T. T. Yan, X. R. Wen, J. P. Zhang, L. Y. Shi and Q. D. Zhong, *J Mater Chem A*, 2013, **1**, 11778-11789.

93. H. B. Li, T. Lu, L. K. Pan, Y. P. Zhang and Z. Sun, *J Mater Chem*, 2009, **19**, 6773-6779.
94. H. B. Li, L. D. Zou, L. K. Pan and Z. Sun, *Environ Sci Technol*, 2010, **44**, 8692-8697.
- 5 95. X. R. Wen, D. S. Zhang, T. T. Yan, J. P. Zhang and L. Y. Shi, *J Mater Chem A*, 2013, **1**, 12334-12344.
96. Z. Li, B. Song, Z. K. Wu, Z. Y. Lin, Y. G. Yao, K.-S. Moon and C. P. Wong, *Nano Energy*, 2015, **11**, 711-718.
97. H. Bi, F. Q. Huang, J. Liang, Y. F. Tang, X. J. Lu, X. M. Xie and M. H. Jiang, *J Mater Chem*, 2011, **21**, 17366-17370.
- 10 98. B. Tang, G. X. Hu, H. Y. Gao and Z. X. Shi, *J Power Sources*, 2013, **234**, 60-68.
99. Y. C. Yong, X. C. Dong, M. B. Chan-Park, H. Song and P. Chen, *ACS Nano*, 2012, **6**, 2394-2400.
- 15 100. C. G. Hu, H. H. Cheng, Y. Zhao, Y. Hu, Y. Liu, L. M. Dai and L. T. Qu, *Adv Mater*, 2012, **24**, 5493-5498.
101. T. Maiyalagan, X. C. Dong, P. Chen and X. Wang, *J Mater Chem*, 2012, **22**, 5286-5290.
102. F. Su, J. Zeng, X. Bao, Y. Yu, J. Y. Lee and X. S. Zhao, *Chem Mater*, 2005, **17**, 3960-3967.
- 20 103. T. Wu, M. X. Chen, L. Zhang, X. Y. Xu, Y. Liu, J. Yan, W. Wang and J. P. Gao, *J Mater Chem A*, 2013, **1**, 7612-7621.
104. Y. Z. Su, Y. Zhang, X. D. Zhuang, S. Li, D. Q. Wu, F. Zhang and X. L. Feng, *Carbon*, 2013, **62**, 296-301.
- 25 105. S. Chen, J. J. Duan, W. Han and S. Z. Qiao, *Chem Commun*, 2014, **50**, 207-209.
106. Q. Z. Liang, X. X. Yao, W. Wang, Y. Liu and C. P. Wong, *ACS Nano*, 2011, **5**, 2392-2401.
107. M. T. Pettes, H. X. Ji, R. S. Ruoff and L. Shi, *Nano Lett*, 2012, **12**, 2959-2964.
- 30 108. H. S. Ahn, J. M. Kim, C. Park, J. W. Jang, J. S. Lee, H. Kim, M. Kaviani and M. H. Kim, *Sci Rep*, 2013, **3**, 1960.
109. X. F. Zhang, K. K. Yeung, Z. L. Gao, J. K. Li, H. Y. Sun, H. S. Xu, K. Zhang, M. Zhang, Z. B. Chen, M. M. F. Yuen and S. H. Yang, *Carbon*, 2014, **66**, 201-209.
- 35 110. K. Zhang, Y. Chai, M. M. F. Yuen, D. G. W. Xiao and P. C. H. Chan, *Nanotechnology*, 2008, **19**, 215706.
111. H. Chen, M. Chen, J. Di, G. Xu, H. Li and Q. Li, *J Phys Chem C*, 2012, **116**, 3903-3909.
- 40 112. Q. Liang, X. Yao, W. Wang, Y. Liu and C. P. Wong, *ACS Nano*, 2011, **5**, 2392.
113. S. R. Ng, C. X. Guo and C. M. Li, *Electroanalysis*, 2011, **23**, 442-448.
114. L. Zhang, D. B. Tian and J. J. Zhu, *Bioelectrochemistry*, 2008, **74**, 157-163.
- 45 115. C. M. Li, J. Zang, D. Zhan, W. Chen, C. Q. Sun, A. L. Teo, Y. T. Chua, V. S. Lee and S. M. Moochhala, *Electroanalysis*, 2006, **18**, 713-718.
116. F. Yavari, Z. P. Chen, A. V. Thomas, W. C. Ren, H. M. Cheng and N. Koratkar, *Sci Rep*, 2011, **1**, 166.
- 50 117. C. C. Kung, P. Y. Lin, F. J. Buse, Y. H. Xue, X. Yu, L. M. Dai and C. C. Liu, *Biosens Bioelectron*, 2014, **52**, 1-7.
118. M. Yuan, A. P. Liu, M. Zhao, W. J. Dong, T. Y. Zhao, J. J. Wang and W. H. Tang, *Sens Actuators, B*, 2014, **190**, 707-714.
- 55 119. G. Yang, C. Lee and J. Kim, *J Electrochem Soc*, 2013, **160**, B160-B163.
120. T. Yang, Q. Guan, Q. H. Li, L. Meng, L. L. Wang, C. X. Liu and K. Jiao, *J Mater Chem B*, 2013, **1**, 2926-2933.
121. F. Liu, Y. Piao, J. S. Choi and T. S. Seo, *Biosens Bioelectron*, 2013, **50**, 387-392.
- 60 122. F. N. Xi, D. J. Zhao, X. W. Wang and P. Chen, *Electrochem Commun*, 2013, **26**, 81-84.
123. Y. Wang, C. Guan, K. Wang, C. X. Guo and C. M. Li, *J Chem Eng Data*, 2011, **56**, 642-645.
- 65 124. F. Liu, S. Chung, G. Oh and T. S. Seo, *ACS Appl Mater Interfaces*, 2012, **4**, 922-927.
125. H. X. Sun, A. Li, X. J. Qin, Z. Q. Zhu, W. D. Liang, J. An, P. Q. La and W. Q. Deng, *Chemosuschem*, 2013, **6**, 2377-2381.
126. J. Yuan, X. Liu, O. Akbulut, J. Hu, S. L. Suib, J. Kong and F. Stellacci, *Nat. Nanotechnol.*, 2008, **3**, 332-336.
- 70 127. Y. Zhang, S. Wei, F. Liu, Y. Du, S. Liu, Y. Jia, T. Yokoi, T. Tatsumi and F. Xiao, *Nano Today*, 2009, **4**, 135-142.
128. C. Wang, F. Tzeng, H. Chen and C. Chang, *Langmuir*, 2012, **28**, 10015-10019.
- 75 129. D. D. Nguyen, N. Tai, S. Lee and W. Kuo, *Energy Environ Sci*, 2012, **5**, 7908-7912.
130. H. Bi, X. Xie, K. Yin, Y. Zhou, S. Wan, L. He, F. Xu, F. Banhart, L. Sun and R. S. Ruoff, *Adv Funct Mater*, 2012, **22**, 4421-4425.
131. Y. Wang, C. X. Guo, X. Wang, C. Guan, H. B. Yang, K. A. Wang and C. M. Li, *Energy Environ Sci*, 2011, **4**, 195-200.
- 80 132. T. H. Yu, C. W. Liang, C. Kim, E. S. Song and B. Yu, *IEEE Electron Device Lett*, 2011, **32**, 1110-1112.
133. B. J. Kim, G. Yang, M. J. Park, J. S. Kwak, K. H. Baik, D. Kim and J. Kim, *Appl Phys Lett*, 2013, **102**(16): 161902.
- 85 134. N. Li, Q. Zhang, S. Gao, Q. Song, R. Huang, L. Wang, L. W. Liu, J. W. Dai, M. L. Tang and G. S. Cheng, *Sci Rep*, 2013, **3**, 1604.